Chapter 1
Phase transitions in single neurons and neural populations: Critical slowing, anesthesia, and sleep cycles

D.A. Steyn-Ross, M.L. Steyn-Ross, M.T. Wilson, and J.W. Sleigh

1.1 Introduction

It is a matter of common experience that the brain can move between many different major states of vigilance: wakefulness; sleep; trauma- and anesthetic-induced quiet unconsciousness; disease- and drug-induced delirium; epileptic and electrically-induced seizure. By monitoring cortical brain activity with EEG (electroencephalogram) electrodes, it becomes possible to detect more subtle alterations within these major states; for example, we find that natural sleep consists of periodic cyclings between inactive, quiet slow-wave sleep (SWS) and a paradoxically active phase—characterized by rapid eye movements and reduced muscle tone—named REM (rapid-eye-movement) or paradoxical sleep.

The existence of these contrasting brain states motivates us to ask: How does the brain move between states? Is the changing of states a smooth, graduated motion along a trajectory of similar states? Or is the transition more like an abrupt switching choice between two (or more) mutually-exclusive cortical destinations? If the state-change can be thought of as a switching choice, then we might envision a hills-and-valleys cortical landscape in which the crest of a hill represents a decision point, and the two valleys falling away to either side are the alternative destination states. In this picture, we could expect a cortex, delicately poised at a decision point, to exhibit signature behaviors in the statistical properties of its fluctuations as it "ponders" its choices. This notion—that decision points can be identified from critical changes in fluctuation statistics—is a unifying theme that we will return to several times in this chapter.

D. Alistair Steyn-Ross · Moira L. Steyn-Ross · Marcus T. Wilson
Department of Engineering, University of Waikato, P.B. 3105, Hamilton 3240, New Zealand.
e-mail: asr@waikato.ac.nz msr@waikato.ac.nz m.wilson@waikato.ac.nz
http://phys.waikato.ac.nz/cortex

Jamie W. Sleigh
Waikato Clinical School, University of Auckland, Waikato Hospital, Hamilton 3204, New Zealand.
e-mail: sleighj@waikatodhb.govt.nz

The chapter is structured as follows. We examine first a simplified single-neuron model due to Hugh R. Wilson [29, 30] that is able to produce either the arbitrarily slow firing rates (so-called type-I behavior) observed in cortical neurons in the mammalian cortex, or, with a minor change in parameter values, exhibits the sudden-onset firing rates (type-II behavior) that characterize both the squid giant-axon excitable membrane, and the neurons in the mammalian auditory cortex. Our interest here is *not* the above-threshold behaviors such as the shape and time-course of the action potential, nor the functional form of spike-rate on stimulus current; instead, we focus on the sensitivity of the non-firing, but *near-threshold*, resting membrane to small noisy perturbations about its equilibrium resting state as the neuron makes a stochastic exploration of its nearby state-space, exercising what Jirsa and Ghosh[1] describe as its *dynamic repertoire*.

Gross changes in states of brain vigilence, such as from awake to asleep, and from anethetized to aware, reflect alterations in the coordinated, emergent activity of entire populations of neurons, rather than a simple "scaling up" of single-neuron properties. In Sect. 1.3 we examine historical support for the notion that induction of anesthesia can be viewed as a first-order "anesthetodynamic" neural phase transition, comparing biological response to an "obsolete" drug (ether) with a very commonly used modern drug (propofol). We describe EEG response predictions using a noise-driven mean-field cortical model, and identify an explanation for the paradoxical observation that inhibitory agents (such as anesthetics) can have an excitatory effect at low concentrations.

Section 1.4 investigates the SWS–REM sleep cycle, finding similarities in the EEG sleep patterns of the human, the cat, and the fetal sheep. We suggest that the species-independent surge in correlated low-frequency brain activity prior to transition into REM sleep can be explained in terms of a first-order jump from a hyperpolarized quiescent state (SWS) to a depolarized active state (REM).

In Sect. 1.5 we examine the recently published Fulcher–Phillips–Robinson model [18, 19] for the wake–sleep cycle, demonstrating a divergent increase in brain sensitivity at the transition point: the occurrence of a peak in neural susceptibility may provide a natural explanation for the so-called "hypnagogic jerk"—the falling or jolting sensation frequently experienced at the point of falling asleep.

We summarize the common threads running through these neuron and neural population models in Sect. 1.6.

1.2 Phase transitions in single neurons

In the absence of noise, a single neuron is bistable: it is either at rest or generating an action potential. As noted by Freeman [6], the approach to firing threshold is heralded by an increasing sensitivity to stimulus:

[1] See Chap. 4 of this volume.

> When a depolarizing current is applied in very small steps far from threshold, the neural dynamics is linear; responses to current steps are additive and proportional to the input [...] As threshold is approached, a nonlinear domain is encountered in which local responses occur that are greater than expected by proportionality.

The fact that a biological neuron is constantly buffeted to a background wash of low-level noisy currents allows the neuron to explore its local state space. These stochastic explorations can be tracked by monitoring the voltage fluctuations at the soma. We will show that the statistics of these fluctuations change—in characteristic ways—as the critical point for transition to firing is approached.

1.2.1 H.R. Wilson spiking neuron model

The H.R. Wilson equations [29, 30] describe neuron spiking dynamics in terms of a pair of first-order coupled differential equations,

$$C\frac{dV}{dt} = I_{\rm Na}(t) + I_{\rm K}(t) + I_{\rm dc} + I_{\rm noise}(t)\,, \tag{1.1}$$

$$\tau\frac{dR}{dt} = -R(t) + R_\infty(V) + R_{\rm noise}(t)\,. \tag{1.2}$$

The neuron is pictured as a "leaky" capacitance C whose interior voltage V is determined by sum of ionic ($I_{\rm Na}$, $I_{\rm K}$) and injected ($I_{\rm dc}$) currents entering the lipid membrane. Here we have supplemented the original Wilson form by adding white-noise perturbations ($I_{\rm noise}$, $R_{\rm noise}$) to the current (1.1) and recovery-variable (1.2) equations.

The sodium (Na) and potassium (K) ionic currents are determined by their respective conductances ($g_{\rm Na}$, $g_{\rm K}$) and reversal potentials ($E_{\rm Na}$, $E_{\rm K}$),

$$I_{\rm Na}(t) = -g_{\rm Na}(V)(V-E_{\rm Na})\,, \qquad I_{\rm K}(t) = -g_{\rm K}R\cdot(V-E_{\rm K})\,, \tag{1.3}$$

where R is the recovery variable that approximates the combined effects of potassium activation and sodium inactivation that dominate the slower neuron dynamics for the return to rest following the fast up-stroke of an action potential. Definitions and constants for the H.R. Wilson model are listed in Table 1.1.

Comparing Eqs (1.1–1.3) against Hodgkin and Huxley's (HH) classic four-variable model for the excitable membrane of the squid giant-axon [11], we see the significant simplifications Wilson has made to the complicated HH forms for the time- and voltage-dependence of sodium and potassium conductances: the sodium conductance $g_{\rm Na}$ is now a quadratic function of membrane voltage; the potassium conductance $g_{\rm K}$ becomes a constant; and the steady-state for the combined potassium activation/sodium inactivation is either a quadratic (for type-I spiking behavior), or linear (type-II spiking), function of voltage. These simplifications reduce the dimensionality of the neuron from four dynamic variables to two—while preserving

Table 1.1 Definitions and constants for stochastic implementation of the H. R. Wilson [30] model for type-I (mammalian) and type-II (squid) excitable membrane. $I_{\rm dc}^{\rm crit}$ is the threshold input current for spike generation.

Description	Symbol	Type-I (mammal)	Type-II (squid)	Unit
Capacitance	C	1.0	0.8	μF cm^{-2}
Time-constant	τ	5.6	1.9	ms
Reversal potentials	$E_{\rm Na}$, $E_{\rm K}$	$+48$, -95	$+55$, -92	mV
K$^+$ conductance	$g_{\rm K}$	26.0	26.0	mS cm^{-2}
Noise-scale (current)	σ_I	1.0	0.1	μA cm^{-2} (ms)$^{1/2}$
Noise-scale (recovery)	σ_R	1.0	0.1	(ms)$^{1/2}$
Threshold current	$I_{\rm dc}^{\rm crit}$	$\sim$21.4752886	$\sim$7.77327142	μA cm^{-2}
Na$^+$ conductance, $g_{\rm Na}(V) = a_2V^2 + a_1V + a_0$				
	a_2	33.80×10^{-4}	32.63×10^{-4}	mS cm^{-2} mV^{-2}
	a_1	47.58×10^{-2}	47.71×10^{-2}	mS cm^{-2} mV^{-1}
	a_0	17.81	17.81	mS cm^{-2}
Recovery steady-state, $R_\infty(V) = b_2V^2 + b_1V + b_0$				
	b_2	3.30	0	mV^{-2}
	b_1	3.798	1.35	mV^{-1}
	b_0	1.26652	1.03	–

some essential biophysics[2]—making the model much more amenable to mathematical analysis and insight.

The additive noises appearing on the right of Eqs (1.1) and (1.2) are two independent time-series of white-noise perturbations that are supposed to represent the continuous random buffeting of the soma and recovery processes within a living, biological neuron. The noises are defined as,

$$I_{\rm noise}(t) \,=\, \sigma_I\,\xi_I(t)\,, \qquad R_{\rm noise}(t) \,=\, \sigma_R\,\xi_R(t)\,, \tag{1.4}$$

where σ_I, σ_R are the rms noise scale-factors for current and recovery respectively, and ξ_I, ξ_R are zero-mean, Gaussian-distributed delta-correlated white-noise sources with statistics,

$$\langle\xi(t)\rangle \,=\, 0\,, \qquad \langle\xi_i(t)\,\xi_j(t')\rangle \,=\, \delta_{ij}\,\delta(t-t')\,. \tag{1.5}$$

Here, δ_{ij} is the dimensionless Kronecker delta and $\delta(t)$ is the Dirac delta function carrying dimensions of inverse time. The $\xi(t)$ are approximated in simulation by the construction

$$\xi(t) \,=\, \mathscr{N}(0,1)/\sqrt{\Delta t}\,, \tag{1.6}$$

[2] Notably: ionic reversal potentials, and the implicit Ohm's-law dependence of ionic current on the signed displacement of the membrane voltage from the reversal values.

where Δt is the size of the time-step, and $\mathscr{N}(0,1)$ denotes a normally-distributed random-number sequence of mean zero, variance unity. In the numerical experiments described below, the noise amplitudes are set at a sufficiently small value to ensure that the neuron is allowed to explore its near steady-state subthreshold (i.e., non-firing) state space; in this regime we will find that, as firing threshold is approached from below, the subthreshold fluctuations become *critically slowed*, exactly as predicted by small-noise linear stochastic theory.

1.2.2 Type-I and type-II subthreshold fluctuations

Excitable membranes are classified according to the nature of their spiking onset. For the squid axon and for auditory nerve cells, action potential oscillations emerge at a non-zero frequency when an injected dc stimulus current exceeds threshold; such membranes are classified as being type-II or *resonator* [12]. In contrast, for type-I or *integrator* membranes (e.g., human cortical neurons), spike oscillations emerge at zero frequency as the current stimulus crosses threshold—that is, the firing frequency in a type-I neuron can be arbitrarily slow. By altering the voltage dependence of R_∞ (the steady-state value for the recovery variable in Eq. (1.2)) from linear to quadratic, the H.R. Wilson model neuron can be transformed from a resonator into an integrator (see Table 1.1 for polynomial coefficients).

Figure 1.1 compares the near-threshold behavior of the Wilson resonator neuron (Fig. 1.1(a)) with that of the integrator neuron (Fig. 1.1(b)) for white-noise perturbations superimposed on five different levels of constant stimulus current $I_{\rm dc}$. For the squid-axon type-II resonator, the voltage fluctuations show an increasing tendency to "ring" at a characteristic frequency, with the ringing events becoming more prolonged and pronounced as the critical level of drive current $I_{\rm dc}^{\rm crit} \approx 7.7732\ \mu{\rm A/cm}^2$ is approached from below.

In contrast, the mammalian type-I integrator shows voltage fluctuations that become simultaneously larger and slower as the drive current approaches the critical value $I_{\rm dc}^{\rm crit} \approx 21.4752\ \mu{\rm A/cm}^2$. One is reminded of Carmichael's eloquent description of a state change in quantum optics in which the process [1],

> ... amplifies the initial fluctuations up to the macroscopic scale, making it impossible to disentangle a mean motion from the fluctuations.

Prior to spike onset, is the slowly varying trend a fluctuation about the mean, or the mean motion itself? At the critical point leading to the birth of an action potential in an integrator neuron, the mean motion *is* the fluctuation.

In order to better appreciate the underlying statistical trends in fluctuation variability as the critical stimulus current is approached, we repeat the 200-ms numerical simulations of the stochastic Wilson equations (1.1)–(1.2) a total of 2000 times, each run using a different constant value of $I_{\rm dc}$. These $I_{\rm dc}$ stimulus values, in $\mu{\rm A/cm}^2$, are evenly distributed over the range -10 to $+7.77$ for the resonator experiments (see Fig. 1.2(a)), and -10 to $+21.475$ for the integrator experiments

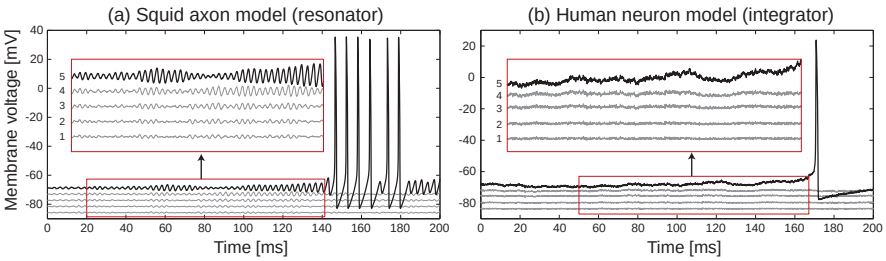

Fig. 1.1 Stochastic simulations for the H.R. Wilson models for (a) squid axon (type-II) and (b) human cortical (type-I) neuron. Framed insets show detail of the subthreshold voltage fluctuations prior to spike onset. (a) Numbered from bottom to top, the five squid stimulation currents are $I_{\rm dc} = 0, 2, 4, 6, 7.7\ \mu$A/cm^2. (To improve visibility, the squid traces have been displaced vertically by $(4m-20)$ mV where $m = 1\ldots5$ is the curve number.) (b) Cortical neuron stimulation currents are (bottom to top) $I_{\rm dc} = -100, -40, 0, +16, +21.4752\ \mu$A/cm^2. Integration algorithm is semi-implicit Euler-trapezium with timestep $\Delta t = 0.005$ ms. All runs within a given figure used the same sequence of 40 000 Gaussian-distributed random-number pairs to generate the white-noise perturbations. (Reproduced from [22].)

(Fig. 1.3(a)). Despite the fact that the variances (σ_I^2, σ_R^2) of the white-noise perturbations remained unchanged throughout these series of experiments, it is very clear that—for both classes of excitable membrane—the variance of the resulting fluctuations *increases strongly and nonlinearly* as the critical value of dc control current is approached, confirming Freeman's earlier observation of growing non-proportionality of response for a neuron near spiking theshold.

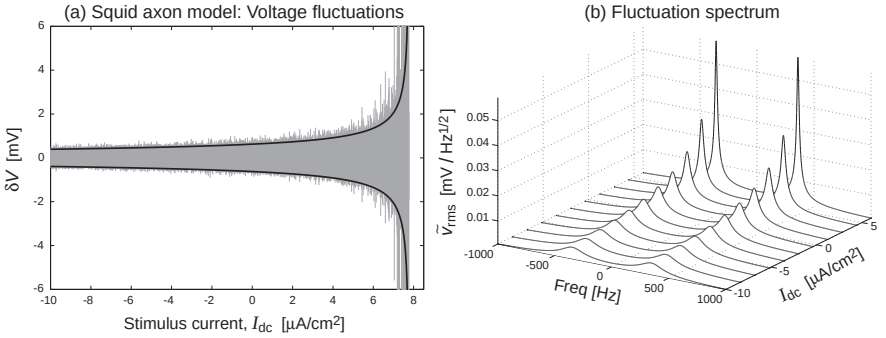

Fig. 1.2 H.R. Wilson type-II (resonator) response to white-noise perturbation as a function of subthreshold stimulus current $I_{\rm dc}$. (a) Each vertical gray stripe shows maximum voltage excursions recorded in a 200-ms stochastic simulation of Eqs (1.1), (1.2) at each of 2000 settings for stimulus current ranging from -10.0 to $+7.77\ \mu$A/cm^2. Solid black curves show theoretical $\pm3\sigma$ limits for voltage excursions away from equilibrium. (b) Theoretical spectral response to white-noise driving for the squid-axon model. The double-sided spectrum develops a pronounced and increasingly narrow resonance at $\sim\pm360$ Hz as the critical current is approached from below. (Reproduced from [22].)

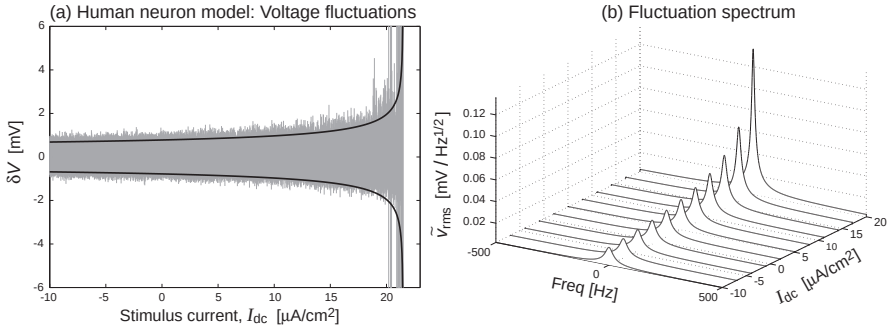

Fig. 1.3 H.R. Wilson type-I (integrator) response to white-noise perturbation as a function of subthreshold stimulus current I_{dc}. (a) Caption as for Fig. 1.2(a), but here stimulus current ranges from -10.0 to $+21.475$ μA/cm^2. Black curves are $\pm 3\sigma$ predictions; gray background verticals indicate fluctuation extrema recorded from 2000 independent numerical experiments. (b) Theoretical spectrum for subthreshold cortical neuron shows a strong resonance developing at *zero* frequency as threshold current for spiking is approached from below. (Reproduced from [22].)

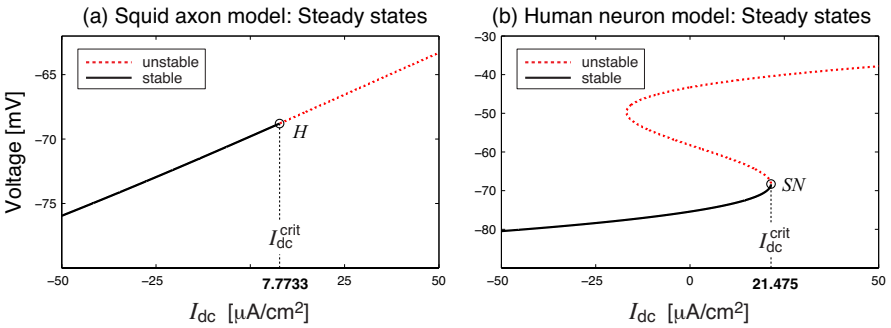

Fig. 1.4 Distribution of steady-state membrane voltages as a function of dc stimulus current I_{dc} for (a) Wilson type-II resonator model; and (b) Wilson type-I integrator neuron. The critical current I_{dc}^{crit} is determined by the point at which the (real part of the) dominant eigenvalue becomes positive, heralding emergence of instability (generation of action potentials). Transition occurs (a) via subcritical Hopf bifurcation at *H* for the resonantor [30]; and (b) via saddle–node annihilation at *SN* for the integrator. (Modified from [22].)

1.2.3 Theoretical fluctuation statistics for approach to criticality

Provided the white-noise perturbations are kept sufficiently small, it is possible to compute *exact* expressions for the variance, power spectrum, and correlation function of the voltage and recovery-variable fluctuations. By "sufficiently small", we mean that the neuron remains subthreshold (i.e., does not generate an action potential spike), so can be accurately described using linear Ornstein–Uhlenbeck (Brownian motion) stochastic theory.

The analysis was detailed in Ref. [22], but in outline, proceeds as follows. For a given (subthreshold) value of stimulus current $I_{\rm dc}$, compute the steady-state coordinate $(V^{\rm o}, R^{\rm o})$. For the H.R. Wilson resonator, $V^{\rm o}$ is a monotonic increasing function of $I_{\rm dc}$ (see Fig. 1.4(a)), whereas for the Wilson integrator the graph of $V^{\rm o}$ vs $I_{\rm dc}$ maps out an S-shaped curve (Fig. 1.4(b)), so there can be up to three steady states for a given value of stimulus current [30]—in which case, select the steady state with the lowest voltage.

We rewrite the Wilson equations (1.1), (1.2) in their deterministic (noise-free) form,

$$F_1(V,R) \equiv (I_{\rm Na} + I_{\rm K} + I_{\rm dc})/C, \tag{1.7}$$

$$F_2(V,R) \equiv (-R(t) + R_\infty(V))/\tau, \tag{1.8}$$

and linearize these by expressing the fluctuations (v,r) as small deviations away from steady state $(V^{\rm o}, R^{\rm o})$,

$$v(t) = V(t) - V^{\rm o}, \qquad r(t) = R(t) - R^{\rm o}, \tag{1.9}$$

Reinstating the additive noise terms, the linearized Wilson equations become coupled Brownian motions of the form,

$$\frac{d}{dt}\begin{bmatrix} v \\ r \end{bmatrix} = \mathbf{J}\begin{bmatrix} v \\ r \end{bmatrix} + \sqrt{\mathbf{D}}\begin{bmatrix} \xi_I \\ \xi_R \end{bmatrix}, \tag{1.10}$$

with Jacobian and diffusion matrices defined respectively by,

$$\mathbf{J} = \left.\begin{bmatrix} \frac{\partial F_1}{\partial V} & \frac{\partial F_1}{\partial R} \\ \frac{\partial F_2}{\partial V} & \frac{\partial F_2}{\partial R} \end{bmatrix}\right|_{(V^{\rm o}, R^{\rm o})}, \qquad \mathbf{D} = \begin{bmatrix} \left(\frac{\sigma_I}{C}\right)^2 & 0 \\ 0 & \left(\frac{\sigma_R}{\tau}\right)^2 \end{bmatrix}, \tag{1.11}$$

where $\mathbf{J}$ is evaluated at the selected equilibrium point.

In the vicinity of an equilibrium point, the deterministic behavior of the two-variable Ornstein–Uhlenbeck system is completely defined by the two eigenvalues, λ_1 and λ_2, belonging to the Jacobian matrix.

For the subthreshold Wilson *resonator*, the eigenvalues are complex, $\lambda_{1,2} = -\alpha \pm i\omega_{\rm o}$, with the damping $\alpha = -{\rm Re}(\lambda)$ being *positive* for a decaying impulse response and a stable equilibrium. If the damping becomes negative (i.e., ${\rm Re}(\lambda) > 0$), a minor disturbance will grow exponentially, signaling onset of nonlinear *super-threshold* behavior (generation of a spike). But if the drive current matches the critical value $I_{\rm dc}^{\rm crit}$ *exactly*, the damping will be precisely zero, thus a small disturbance will provoke a resonant response at frequency $\omega_{\rm o}$ whose oscillations will neither decay nor grow over time, but will persist "forever".

For the Wilson *integrator* neuron, both eigenvalues are purely real, with $\lambda_2 < \lambda_1 < 0$ for a stable equilibrium. Exponential growth leading to spike onset is predicted if the dominant eigenvalue λ_1 becomes positive. At the critical current for the integrator (lower-right turning point in Fig. 1.4(b) labeled *SN*), the unstable mid-

branch saddle equilibrium meets the stable lower-branch node at a saddle–node bifurcation. At this bifurcation point the dominant eigenvalue is precisely zero, leading to a delicate point of balance in which small perturbations are sustained indefinitely, neither decaying back to steady state nor growing inexorably into nonlinearity and thence to a spike. At this point, the neuron response will become *critically slowed*.

1.2.3.1 Fluctuation variance

Following Gardiner's analysis of the multivariate Ornstein–Uhlenbeck process [8], we can write theoretical expressions of the white-noise evoked fluctuation variance and spectrum, and deduce scaling laws for the divergences that manifest at the critical point.

The steady-state variances of the fluctuations developed in the Wilson excitable membrane depend explicitly on the elements of the diffusion matrix and the Jacobian matrix, and on the Jacobian eigenvalues. For the H.R. Wilson type-I integrator, the variance of the voltage fluctuations reads [22],

$$\mathrm{var}\{v\} = \frac{(\lambda_1\lambda_2 + J_{22}^2)D_{11} + J_{12}^2 D_{22}}{-2\,(\lambda_1+\lambda_2)\,\lambda_1\lambda_2} \quad \xrightarrow{\lambda_1\uparrow 0^-} \quad \sim \frac{1}{-\lambda_1} \sim \frac{1}{\sqrt{\varepsilon}}\,. \tag{1.12}$$

Here, λ_1 is the dominant (i.e., least negative) eigenvalue, and both eigenvalues are real. As the dc stimulus current approaches its critical value, λ_1 approaches zero from below. Thus, at the threshold for spiking, the integrator neuron becomes infinitely responsive to white-noise perturbation with the fluctuation power diverging to infinity. The scaling for this divergence follows an $\varepsilon^{-1/2}$ power-law, where $\varepsilon = (I_{\mathrm{dc}}^{\mathrm{crit}} - I_{\mathrm{dc}})/I_{\mathrm{dc}}^{\mathrm{crit}}$ is a dimensionless measure of distance from criticality. This is the case because in the vicinity of the saddle–node bifurcation point, the dominant eigenvalue scales as $\sqrt{\varepsilon}$ in a locally parabolic relationship. Since the inverse of the dominant eigenvalue defines the dominant time-scale T for system response, it follows that the characteristic times (correlation time, passage time) will obey the same scaling law: $T \sim \varepsilon^{-1/2}$. We note that this inverse square-root scaling law is a very general feature of systems that are close to a saddle–node bifurcation [26].

For the case of the Wilson type-II resonator, the eigenvalues form a complex conjugate pair, $\lambda_{1,2} = -\alpha \pm i\omega_{\mathrm{o}}$, so the expression for voltage variance becomes [22],

$$\mathrm{var}\{v\} = \frac{(\alpha^2 + \omega_{\mathrm{o}}^2 + J_{22}^2)D_{11} + J_{12}^2 D_{22}}{4\alpha\,(\alpha^2+\omega_{\mathrm{o}}^2)} \quad \xrightarrow{\alpha\downarrow 0^+} \quad \sim \frac{1}{\alpha} \sim \frac{1}{\varepsilon}\,. \tag{1.13}$$

As the critical point is approached, the damping $\alpha = -\mathrm{Re}(\lambda)$ goes to zero from above, leading to a prediction of a divergent power increase that scales as ε^{-1} (for the Wilson resonator close to threshold, α scales *linearly* with ε).

Equations (1.12) and (1.13) were used to compute the theoretical $\pm 3\sigma$ voltage fluctuation limits plotted in Figs 1.3(a) and 1.2(a) respectively; we note excellent

agreement between simulation (gray stripes) and small-noise linear theory (black curves).

1.2.3.2 Fluctuation spectrum

The stationary spectrum for the membrane-voltage fluctuations in the stochastic H.R. Wilson neuron is given by the S_{11} entry of the 2×2 spectrum matrix of the two-variable Ornstein–Uhlenbeck process [8,22]. For the Wilson integrator neuron,

$$S_{11}(\omega) = \frac{1}{2\pi}\frac{J_{22}^2 D_{11} + J_{12}^2 D_{22} + D_{11}\omega^2}{(\lambda_1\lambda_2 - \omega^2)^2 + (\lambda_1+\lambda_2)^2\,\omega^2} \quad \underset{\omega\to 0}{\overset{\lambda_1=0}{\longrightarrow}} \quad \sim \frac{1}{\omega^2}\,. \tag{1.14}$$

The spectral character of the fluctuations changes as the $I_{\rm dc}$ stimulus current increases towards the critical value $I_{\rm dc}^{\rm crit}$, and the corresponding lower-branch steady state moves closer to the saddle–node critical point (marked *SN* in Fig. 1.4(b)): the dominant eigenvalue λ_1 tends to zero from below, causing the power spectral density to diverge at zero frequency, obeying an asymptotic power-law $\sim 1/\omega^2$. Thus, at the critical saddle–node annihilation point, the Wilson integrator is predicted to become "resonant at dc". This spectral tuning of fluctuation energy towards zero frequency is illustrated in the plots of Eq. (1.14) graphed in Fig. 1.3(b).

The noise-driven time-series for the squid-axon model illustrated in Fig. 1.1(a) shows a strongly increasing tendency for the voltage trace to "ring" at a characteristic frequency as the drive current is increased towards the threshold for spiking. This ringing behavior is precisely consistent with the spectrum predicted from Ornstein–Uhlenbeck theory for the Wilson resonator neuron [22],

$$S_{11}(\omega) = \frac{1}{2\pi}\frac{J_{22}^2 D_{11} + J_{12}^2 D_{22} + D_{11}\omega^2}{(\alpha^2+\omega_{\rm o}^2-\omega^2)^2 + 4\alpha^2\omega^2} \quad \underset{\omega\to\omega_0}{\overset{\alpha=0}{\longrightarrow}} \quad \sim \frac{1}{(\omega-\omega_{\rm o})^2}\,, \tag{1.15}$$

implying perfect resonant behavior at frequency $\omega = \omega_{\rm o}$, with the approach to resonance following an asymptotic scaling-law $\sim 1/\delta^2$ where $\delta = (\omega - \omega_{\rm o})$ is the spectral distance from resonance. The resonator spectrum of Eq. (1.15) is plotted in Fig. 1.2(b).

We now move from consideration of single neurons to the gross behaviors of *large populations* of neurons. Just as a single neuron displays telltale nonlinear increases in responsiveness as it approaches the transition point separating stochastic quiescence from dynamic spiking, we find that the collective behaviors of cooperating neuron populations also exhibit characteristic critical responses as the neural population approaches a change of state. We consider three gross changes of cortical state that are easily detected with a single pair of EEG electrodes: induction of anesthesia; natural sleep cycling from slow-wave sleep into REM sleep; and the nightly transition between wake and sleep.

1.3 The anesthesia state

The ability to render a patient safely and reversibly unconscious via administration of an anesthetic drug is an essential component of modern surgical medicine. Although anesthetic agents have been in use for over 160 years, their mode of action remains poorly understood, and is the focus of ongoing and intensive research.

The state of *general anesthesia* is a controlled and reversible unconsciousness characterized by a lack of pain sensation (analgesia), lack of memory (amnesia), muscle relaxation, and depressed reflex responses. In his classic 1937 textbook for anesthetists [9], Arthur Guedel identified four distinct stages in the induction of general anesthesia using the volatile agent diethyl ether:

1. Analgesia and amnesia Patient experiences pain relief and dreamy disorientation, but remains conscious.

2. Delirium Patient has lost consciousness, blood pressure rises, breathing can become irregular, pupils dilate. Sometimes there is breath-holding, swallowing, uncontrolled violent movement, vomiting, and uninhibited response to stimuli.

3. Surgical anesthesia Return of regular breathing, relaxation of skeletal muscles, eye movements slow, then stop. This is the level at which surgery is safe.

4. Respiratory paralysis Anesthetic crisis—respiratory and other vital control centres cease to function, death from circulatory collapse will follow without assisted ventilation and circulatory support.

One might anticipate a roughly linear dose–response in which increasing drug concentration leads to proportionate reductions in brain activity—unfortunately, this simple intuition is immediately contradicted by the anomalous patient response reported by Guedel at the stage-2 (delirium) level of anesthesia. A general anesthetic is administered with the aim of quieting or *inhibiting* brain response to noxious stimuli, and yet, on route to the stage-3 fully-inhibited state, the patient transits through a "wild" uncontrolled state of delirium and *uninhibited* response to stimuli. This is a most interesting paradox: the end-state of inhibition is preceded by an intermediate stage of excitation.

1.3.1 Effect of anesthetics on bioluminescence

In the 1970s, researchers reported that the volatile anesthetics ether, halothane, chloroform, and cyclopropane all reversibly reduce the intensity of light emissions from luminescent bacteria [10, 28]. This followed earlier work by Ueda [27] showing that the light emission from the firefly lantern-extract luciferase was reversibly suppressed by both ether and halothane. The anesthetic concentration required to depress bioluminescent intensity by 50% was found to be very similar to the concentrations required for clinical induction in humans. Because of this remarkable scale-invariance (i.e., the light-emitting complex in photo-bacteria and in fireflies,

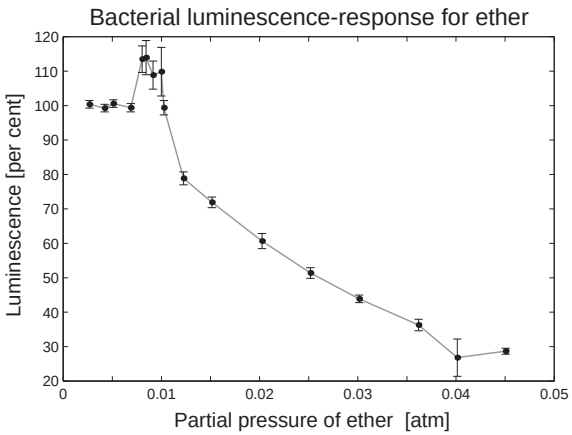

Fig. 1.5 Dose–response curve showing the effect of the volatile anesthetic ether on the luminous intensity of the bacteria *Photobacterium phosphoreum*. Note the anomalous surge, and increased variability, in light output at low ether concentration. (Graph reconstructed from [10].)

and the central nervous system in humans, are responsive to similar concentrations of a given anesthetic), and because light intensity can be be easily and accurately measured, bioluminescence provided a useful early means for quantifying and comparing anesthetic potency.

Figure 1.5 shows the bioluminescence dose–response for ether reported by Halsey and Smith [10]. At partial pressure $P = 0.026$ atm, the luminous intensity has reduced to 50% of its original value. This partial pressure is similar to the 0.032 atm value quoted in the paper for the abolition of the righting instinct in 50% of mice exposed to ether.[3] Of particular interest is their observation that luminescence is *stimulated* by low doses of ether ($P \sim 0.009$ atm), confirming an earlier report by White and Dundas [28]. Halsey and Smith [10] stated that stimulation also occurred at low levels of chloroform, halothane, and nitrous oxide (though for the latter two agents the increase was "not statistically significant", presumably because the uncertainty bars became very large during this transition phase).

Although neither research group offered an explanation for this paradoxical excitation by an inhibitory agent, it seems rather likely that the dilute-ether boost in luminous intensity and variability seen in bacteria could be mapped directly to Guedel's delirium (stage-2) for ether-induced anesthesia in human patients—though it might be difficult to test this idea quantitatively now, since diethyl-ether is no longer used as an anesthetic agent in hospitals.

1.3.2 Effect of propofol anesthetic on EEG

Unlike diethyl-ether and the other volatile anesthetic agents (such as those tested in the bioluminescence experiments) that are delivered to the patient by inhalational

[3] Prior to the bioluminescence studies, small mammals had been used to calibrate anesthetic potency.

mask, propofol, a modern and commonly-used general anesthetic, is injected intravenously as a liquid emulsion, so is likely to have a different mode of action. Despite this difference, the onset of propofol anesthesia is also heralded by a *surge* in brain activity that is readily detected as a sudden increase in low-frequency EEG power [14, 15]; this excitation subsides as the patient moves deeper into unconsciousness. Thus propofol, like ether, is "biphasic", being excitatory at low concentrations, then inhibitory at higher concentrations.

The measurements of Kuizenga *et al.* [15] shown in Fig. 1.6(a) show that a *second* surge in activity occurs as the propofol concentration dissipates, allowing the patient to re-emerge into consciousness. Thus there are *two* biphasic peaks per induction–emergence cycle: the first at or near loss-of-consciousness (LOC), and the second at recovery-of-consciousness (ROC). The onset of the first EEG surge lags $\sim$2 min behind the rise in propofol concentration; this delay arises because of the unavoidable mismatch between the site of drug *effect* (the brain) and the site of drug *measurement* (the blood)—it takes about 2 min for the drug to diffuse across the blood–brain barrier. Even after compensating for this delay, there seems to remain a hysteretic separation between that the LOC and ROC biphasic peaks, meaning that the patient awakens at a *lower* drug concentration than that required to put the patient to sleep.

At the individual neuron level, the major effect of propofol is to prolong the duration of inhibitory postsynaptic potential (IPSP) events, thereby increasing the inward flux of chloride ions and thus increasing the hyperpolarizing effectiveness of inhibitory firings by GABAergic interneurons [4, 13].

We developed a model for propofol anesthesia by modifying a set of cortical equations by Liley [16] to include a control parameter λ that lengthens the IPSP decay-contant (by reducing the IPSP rate-constant γ_i) in proportion to drug concentration: $\gamma_i^{-1} \to \lambda\gamma_i^{-1}$; see Refs [23–25] for full details. For a physiologically plausible set of cortical parameters, we found that, for a given value of anesthetic effect λ, the model cortex could support up to *three* homogeneous steady-states; see Fig. 1.6(b). The upper (active) and lower (quiescent) stable nodes are separated by a saddle-branch that is unstable to small perturbations, suggesting the possibility of a propofol-mediated phase transition between the active (conscious) and quiescent (unconscious) states. A transition from active branch A_1-A_2-A_3 to quiescent branch Q_1-Q_2-Q_3 becomes increasingly likely as the node-saddle annihilation point A_3 is approached from the left. The abrupt downward transition represents induction of anesthesia (i.e., LOC).

Once unconscious, reductions in λ allow the cortex to move to the left along the bottom branch of Fig. 1.6(b), with the probability of an upward transition (i.e., ROC) rising as the quiescent node–saddle point Q_1 is approached. Thus the model provides a natural explanation for the observed LOC–ROC drug hysteresis.

Proximity to either of the node–saddle turning points can be detected by the divergent sensitivity of the cortical model to small disturbances. This increasing susceptibility or "irritability" can be quantified by driving the model with low-level white noise, simulating the biological reality of a continuous background wash of unstructured, nonspecific stimulus entering the cortex from the subcortex. Provided

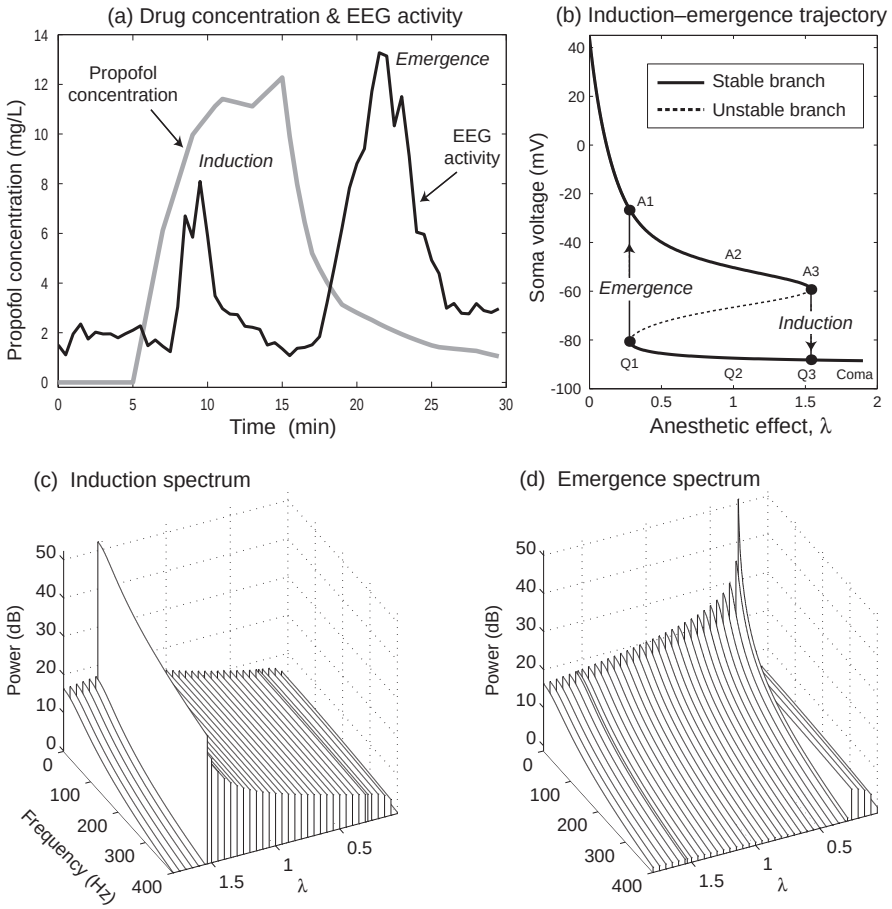

Fig. 1.6 Measured (a) and modeled (b–d) effect of propofol anesthetic agent on EEG activity during induction of, and emergence from, general anesthesia. (a) Time-series showing biphasic surges in 11–15-Hz EEG activity (black curve) in response to increasing and decreasing levels of propofol blood concentration (gray curve) for a patient undergoing a full induction–emergence cycle. [Data provided courtesy of K. Kuizenga.] (b) Trajectory of steady states predicted by a cortical model that assumes propofol acts to prolong IPSP duration by factor λ. Approaches to the saddle-node points A3 (for induction), and Q1 (for emergence), are predicted to show pronounced EEG power surges displayed in (c) and (d) respectively. (Modifed from Figs. 3–5 of [23].)

the intensity of the white-noise stimulus is sufficiently small, we can compute exact expressions for the stationary spectrum and correlation properties of the noise-induced fluctuations by applying stochastic theory [8] to the distribution of eigenvalues obtained from linear stability analysis [23]. The predicted alterations in spectral densities for EEG fluctuation power during anesthetic induction, and during emergence from anesthesia, are plotted in Fig. 1.6(c) and (d) respectively. In both cases, the fluctuation power at zero frequency surges as the node–saddle critical point is

approached, providing advance warning of an impending jump in membrane voltage.

According to this model, we can interpret Kuizenga's observations—of hysteretically separated biphasic surges in EEG activity—as biological evidence supporting the notion that the cortical states of awareness and anesthesia are distinct "phases" of the brain. One could argue that the drug-induced transition into unconsciousness has similarities with physical phase transitions, such as water freezing to ice, with the effect of increasing drug concentration in the brain being analogous to lowering the temperature in the thermodynamic system [25].

1.4 SWS–REM sleep transition

Monitoring the EEG activity of the sleeping human shows natural sleep to consist of two opposed phases: *quiet* slow-wave sleep (SWS) and *active* rapid-eye-movement (REM) sleep. During quiet sleep, the EEG voltage fluctuations are larger, slower—and more coherent across the scalp—than those observed during alert wakefulness. In constrast, during active sleep, the EEG closely resembles wake with its high-frequency, low-amplitude desynchronized patterns. A sleeping adult human cycles between SWS and REM-sleep states at approximately 90-min intervals, for a total of four to six SWS–REM alternations per night.

Figure 1.7 illustrates the cyclic nature of the adult sleep patterns we reported in Ref. [21]. We see four slow surges in EEG power during the six-hour recording, with each surge being terminated by an abrupt decline, signaling the transit from SWS to REM sleep. The increase in fluctuation power is matched by an increase in correlation time[4] that peaks at the end of each SWS episode, with abruptly lower values in REM sleep. This is consistent with the antiphased changes in low- and high-frequency power fractions of Fig. 1.7(c): SWS is associated with increasing low-frequency activity; REM sleep is associated with diminished low-frequency and enhanced high-frequency EEG fluctuations.

The Fig. 1.8 analysis by Destexhe *et al.* [2] for the sleeping cat shows similar patterns of SWS–REM alternation, albeit with a faster cycling time of $\sim$20 min. As was the case for the human sleeper, Fig. 1.8 shows that the sleeping cat exhibits a pronounced increase in low-frequency power prior to transition from SWS into REM. The concomitant increase in "space constant" (correlation *length* for EEG fluctuations) observed for the cat is consistent with an increase in correlation *time* we reported for the human sleeper.

Very similar changes are seen in the ECoG (electrocorticogram) brain activity for a mature fetal sheep. Figure 1.9 shows a 500-s voltage trace, recorded from the cortex of a late-term fetal sheep, that captures the transition between the so-called "high-voltage slow" (i.e., SWS) and "low-voltage fast" (REM sleep) states. As is the case for the human and cat sleepers, the slow-wave state is characterized

[4] Correlation time T is the time-lag required for the autocorrelation function for EEG voltage to decay to $1/e$ of its zero-lag peak.

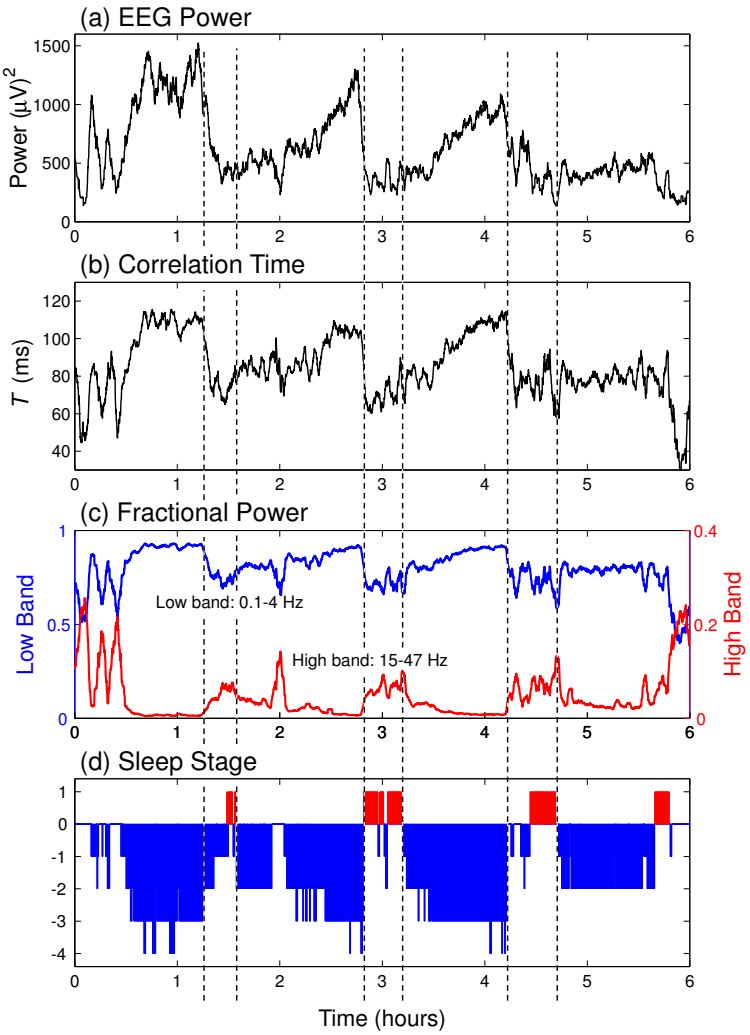

Fig. 1.7 [Color plate] Analysis of an EEG trace recorded from a human sleeper resting overnight in a sleep laboratory. (a) Fluctuation power; (b) correlation time; (c) low- and high-band power fractions; (d) sleep staging as per rulebook of Rechtschaffen and Kale [20]. Key: +1 = REM; 0 = wake; $(-1,-2)$ = light sleep; $(-3,-4)$ = deep sleep (SWS). (Graph reprinted from [21].)

low-frequency correlated fluctuations that increase in intensity and low-frequency content as the point of transition to active sleep is approached.

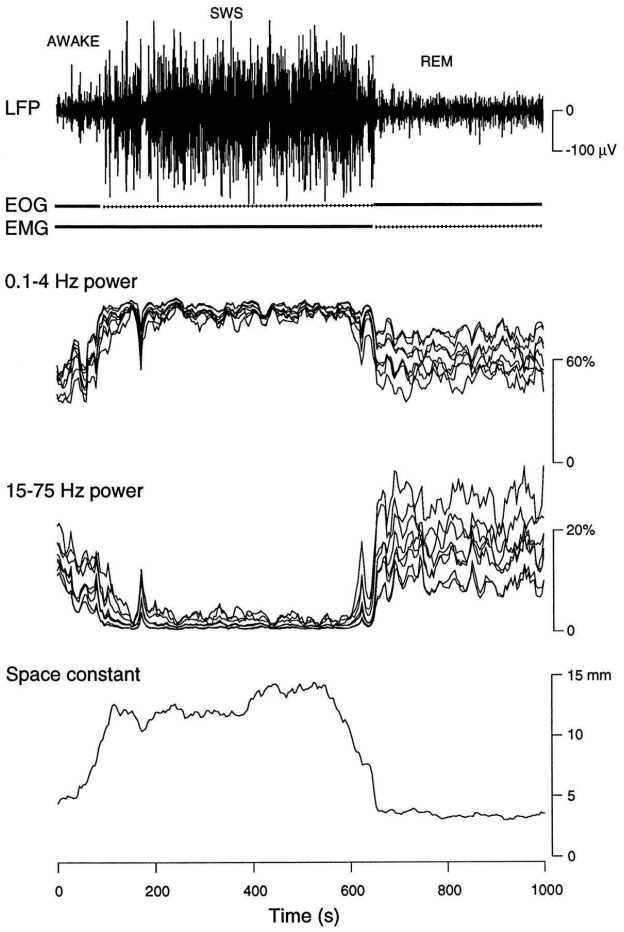

Fig. 1.8 Cortical activity for a cat transitioning from wake to SWS to REM sleep as reported by Destexhe *et al.* [2]. LFP = local field potential (on-cortex EEG); EOG = electrooculogram (eye movement); EMG = electromyogram (muscle tone). REM is identified by reappearance of eye movements (EOG activity) and lack of muscle tone (loss of EMG activity). (Graph reprinted from [2] with permission.)

1.4.1 Modeling the SWS–REM sleep transition

In Ref. [21] we described the construction of a physiologically-based model for the SWS–REM sleep transition that incorporated the two major neuromodulatory influences that are thought to be responsible for the cycles of natural sleep: (a) slow changes in synaptic efficiency ρ_e and resting voltage V_e^{rest} of the population of excitatory neurons caused by the 90-min cycling in acetylcholine (ACh) concentration; and (b) slower changes in resting voltage caused by the gradual elimination during sleep of fatigue agents such as adenosine. The full set of cortical equations are

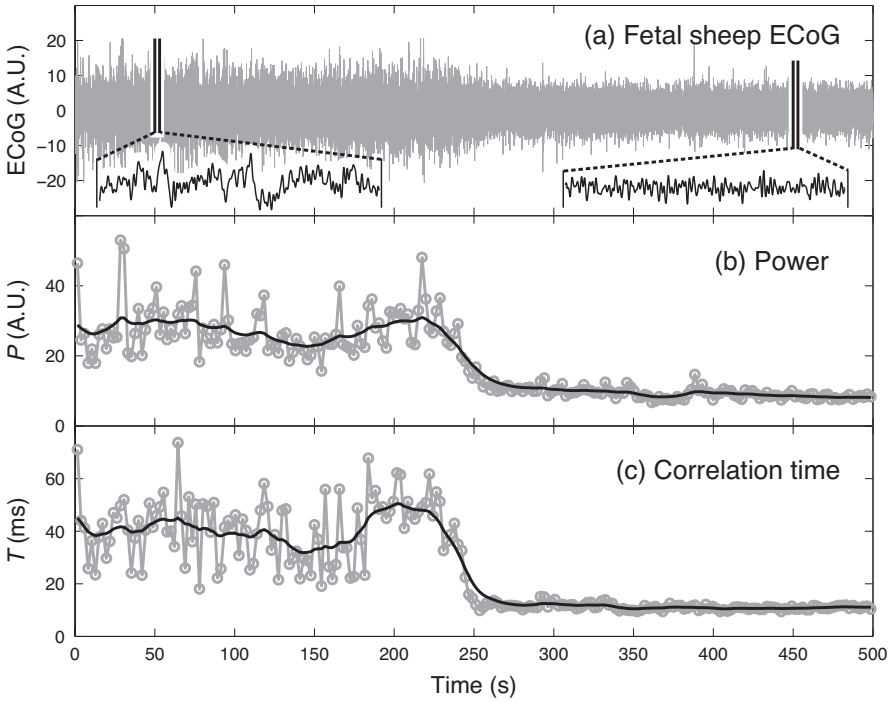

Fig. 1.9 Cortical activity for a full-term fetal sheep (gestational age = 144 days) transitioning from slow sleep (SWS) to active sleep (REM) about 230 s into the recording. (a) ECoG voltage signal (arbitrary units) sampled at 250 s^{-1}. Inserts show 3 s of ECoG signal for the intervals 50–53 s (left), and 450–453 s (right). (b) ECoG power (arbitrary units) computed for 3-s epochs with 25% overlap (gray trace), and smoothed with a Whittaker filter [3] (black trace). (c) ECoG correlation time computed for 3-s epochs with 25% overlap (gray trace), and smoothed with a Whittaker filter (black trace). Note the coincident surge in power and correlation-time prior to transition into REM. (Data provided courtesy of J.J. Wright; analysis by Yanyang Xu.)

described in the chapters by Sleigh *et al* and Wilson *et al*.[5] The model consists of eight differential equations for macrocolumn-averaged soma potentials and synaptic fluxes. Here, we simplify the equations considerably by taking the "slow soma" adiabatic limit in which, relative to the ∼50-ms time-scale of the neuron soma, synaptic input events are assumed to be fast and rapidly equilibrating. This simplification reduces the number of state variables from eight to two: V_e and V_i, the average soma potential for the excitatory and inhibitory neural populations. The acetylcholine and adenosine effects are modeled in terms of λ, a multiplicative factor applied to the ρ_e excitatory synaptic efficiency, and ΔV_e^{rest}, an additive adjustment that tends to depolarize (hyperpolarize) the excitatory membrane potential for positive (negative) values of ΔV_e^{rest}.

[5] See chapters 9 and 10 respectively in the present volume.

The λ and ΔV_e^{rest} parameters define a two-dimensional sleep domain for our cortical model. We located the homogeneous equilibrium states $(V_e^{\text{o}}, V_i^{\text{o}})$ as a function of variations in λ and ΔV_e^{rest}, paying particular attention to those regions of the domain that support multiple (up to three) steady states. When plotted in 3-D, the region of multiple steady states appears as a reentrant fold in the sleep-domain manifold of Fig. 1.10. For our reduced adiabatic cortical model, the top and bottom surfaces of the fold contain stable solutions, and only the middle surface (within the overhang outlined in green) contains unstable solutions.[6]

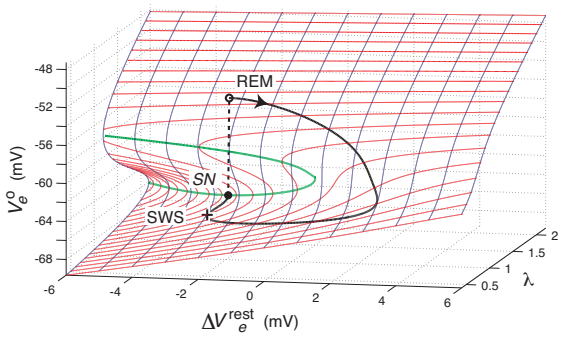

Fig. 1.10 [Color plate] Manifold of homogeneous equilibrium states for SWS–REM sleep-cycling model. Steady-state soma voltage V_e^{o} is plotted as a function of sleep-domain parameters ΔV_e^{rest} and synaptic efficiency λ. The imposed sleep cycle commences in SWS at (+), encounters the saddle–node critical point *SN* (•), and jumps vertically into REM sleep (○). (Modified from [21].)

We impose a cyclic tour of the manifold that is proposed to represent a single 90-min SWS-to-REM-to-SWS sleep cycle. This tour, commencing in the quiescent slow-wave sleep state (marked "+" in Fig. 1.10), proceeds clockwise until it encounters the saddle–node annihilation point *SN* at the lower overhang boundary, whereupon the soma voltage spontaneously makes an upwards jump transition to the activated upper state that we identify as REM sleep.

To visualize the dynamic repertoire available to the sleep-cycling cortex, we perform a numerical simulation of the reduced cortical equations. Voltage fluctuations in soma potential are induced via small-amplitude white-noise stimulations entering the model via the subcortical terms (see [21] for details). The noise-stimulated voltage fluctuations have an amplitude and spectral character that are strongly dependent on the cortical steady-state coordinate. In Fig. 1.11 we have started the numerical simulation very close to the saddle–node critical point *SN* on the bottom branch of Fig. 1.10. Proximity to the critical point causes the fluctuations to be large and slow; after about 2 s, the fluctuation carries the cortex beyond the basin of attraction of the bottom-branch equilibrium point, and the cortex is promptly drawn to the upper state. Fig. 1.11 shows an abrupt loss of low-frequency activity once the model cortex has transited from SWS into the REM (upper) state, similar to the

[6] Analysis of the full nonadiabatic cortical model shows that, for particular choices of synaptic parameters, the regions of instability can extend beyond the overhang, leading to Hopf and wave instabilities. See chapters 9 (Sleigh *et al*) and 10 (Wilson *et al*) for details.

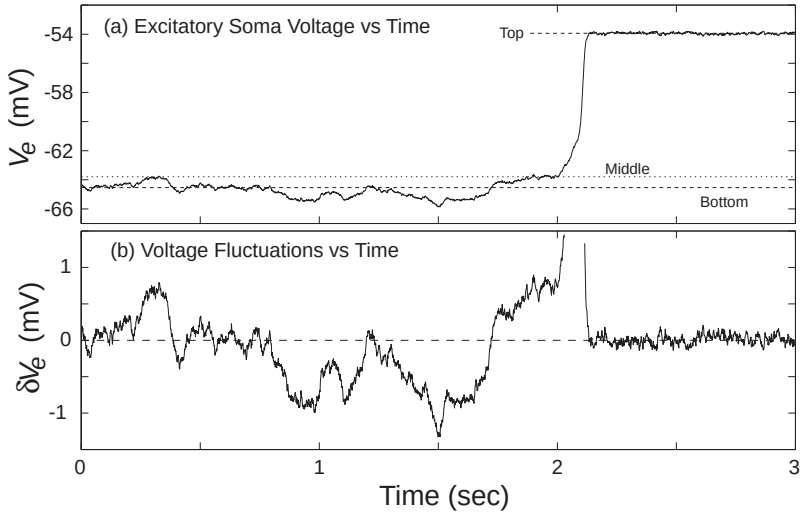

Fig. 1.11 Stochastic simulation of the slow-soma cortical model for SWS–REM sleep cycling. The cortical model is started close to the saddle–node critical point *SN* on the bottom branch of Fig. 1.10. (a) Soma voltage V_e, and (b) noise-induced fluctuations δV_e versus time. Fluctuations in (b) are measured relative to the bottom (top) steady state for times $t < 2.1$ ($t > 2.1$) s. (Modified from [21].)

spectral changes observed in the EEG for human, cat, and fetal-sheep sleep records (Figs 1.7–1.9 respectively).

1.5 The hypnic jerk and the wake–sleep transition

The daily cycling of brain state between wake and sleep is a natural phase transition that is synchronized by the diurnal light cycle and regulated by waxing and waning concentrations of neuromodulators such as acetylcholine (ACh) and adenosine. Fulcher, Phillips, and Robinson (FPR) [7, 18] have developed a model for the wake–sleep transition[7] that we examine briefly here, focusing on the possibility that critical slowing of noise-evoked fluctuations in the wake–sleep control center might provide a natural explanation for the puzzling but common observation of a bodily jerk at the onset of sleep.

The FPR wake–sleep model is expressed in terms of the mutual inhibition between two brainstem neural populations: the *sleep-active* ventrolateral preoptic area (VLPO), and the *wake-active* monoaminergic group (MA). The mutual competition between these populations produces bistable flip-flop behavior that causes the brain state to alternate between wake and sleep states. In the simplest form of the model (Fig. 1.12), the external ACh drive promoting arousal of the MA (and of the

[7] And see Chap. 8 of this volume.

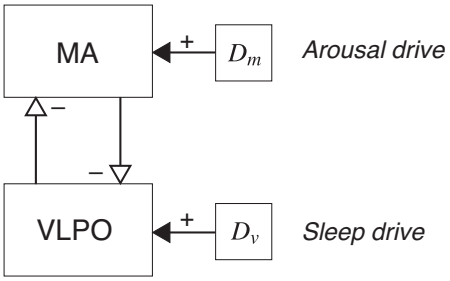

Fig. 1.12 Schematic for simplified Fulcher–Phillips–Robinson model of the sleep–wake switch. Excitatory (+) and inhibitory (–) interactions are shown with solid and outline arrowheads. Mutual inhibition between VLPO and MA neuron populations results in flip-flop bistability between wake and sleep states.

cortex) is replaced by a constant excitation voltage $D_m = A = \text{const.}$, and the external somnogenic and circadian sleep-promoting drives that activate the VLPO are replaced by a slowly-varying control parameter D_v. For this reduced case, the respective equations of motion for V_v and V_m, the VLPO and MA population voltages (relative to resting voltage) become,

$$\frac{dV_v}{dt} = \frac{1}{\tau}\left(-V_v + \nu_{vm}Q_m + D_v\right), \tag{1.16}$$

$$\frac{dV_m}{dt} = \frac{1}{\tau}\left(-V_m + \nu_{mv}Q_v + A\right), \tag{1.17}$$

where τ is a time-constant, ν_{jk} is the coupling strength from population k to j (with $j,k = v$ or m), and Q_k is the sigmoidal mapping from soma voltage V_k to average firing rate [5],

$$Q_k = S(V_k) = Q_{\max}/\left[1+\exp(-\{V_k-\theta\}/\sigma')\right], \tag{1.18}$$

with $Q_{\max}$ being the maximum firing rate, θ the threshold voltage (relative to rest) for firing, and σ' a measure of its spread. (Refer to Table 8.2 for parameter values.)

Setting the time-derivatives in Eqs (1.16–1.17) to zero and solving numerically for the steady states as a function of sleep drive D_v reveals a three-branch locus of equilibria (Fig. 1.13); linear stability analysis indicates that the middle branch is unstable. The top branch has higher V_m values, so is identified with the wake state, while the bottom branch, with lower V_m values, corresponds to sleep. Because the top branch terminates in a saddle–node critical point (SN_1), any noise present in the VLPO–MA flip-flop will produce exaggeratedly enlarged and slowed voltage fluctuations as the awake brain moves to the right along the top branch under the influence of increasing sleep pressure D_v. If D_v^0 is the value of sleep pressure at which the wake state loses stability (i.e., at SN_1), then Eq. (1.12) predicts that the variance of the voltage fluctuations will diverge according to the scaling law

$$\text{var}(V_m) \sim \frac{1}{\sqrt{\varepsilon}}, \tag{1.19}$$

where $\varepsilon = |D_v - D_v^0|$ measures the distance to the saddle–node bifurcation point. This theoretical prediction has been verified by numerical simulation—see Fig. 8.9(a) in the chapter by Robinson *et al* (present volume).

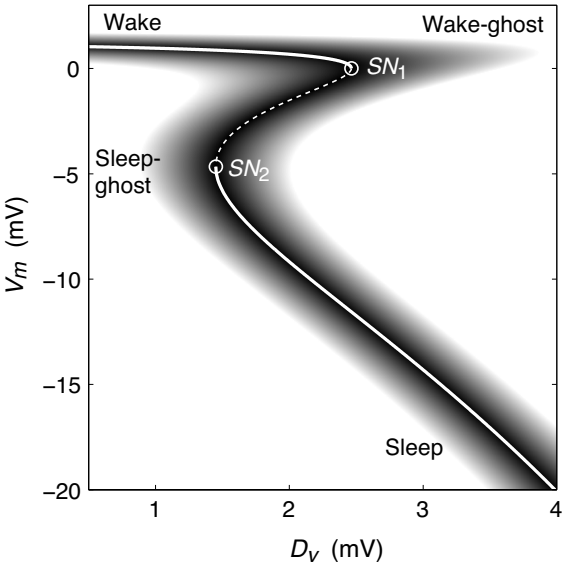

Fig. 1.13 Locus of equilibrium states, saddle–nodes, and ghosts for FPR sleep model as a function of VLPO sleep-drive D_v. White curve shows distribution of stable (solid line) and unstable (dashed line) steady states. Saddle–node bifurcation points SN_1, SN_2 are marked with open circles (○). Regions of slow dynamics are shaded from $\dot{V} = 0$ (black) to $\dot{V} > 0.05$ mV/ms (white). Saddle–node ghosts form in the "shadow zone" that projects beyond the turning points. (Figure modeled on, and modified from, Fulcher *et al* [7].)

It is likely that the brainstem VLPO–MA wake–sleep system projects to other brain areas such as the cerebral cortex and motor cortex. At the point of falling asleep, the VLPO–MA system is close to an instability point, so is highly sensitive to stimulus, thus a sudden impulsive stimulus—either internal (e.g., a spontaneous neural firing) or external (e.g., a sudden noise)—could produce an extravagantly large response. If this disproportionate response were to be transmitted to higher brain areas such as the motor cortex, then we might expect to observe a violent whole-body twitch at or near the transition into sleep. This is a common point-of-sleep experience for many individuals [17], and is known as the *hypnagogic myoclonic twitch* or *hypnic jerk*, but until now has lacked a satisfactory explanation.

The lower-branch turning point SN_2 on Fig. 1.13 marks the position where the sleep state loses stability during the *awakening* phase as the sleep drive D_v reduces in intensity at the end of the diurnal sleep cycle. The fact that this second critical point (for emergence from sleep) occurs at a *lower* value of sleep drive than that required for transition into sleep provides a protective hysteresis that enhances the stability of both states [7, 18]: once asleep, one will tend to remain asleep, and vice versa. Further, if the flip-flop sleep bistability model is correct, we should expect a second nonlinear increase in stimulus sensitivity as the sleep-emerging brain approaches the lower-branch saddle–node critical point. Thus the model predicts that a minor stimulus presented to an almost-awake brain could evoke a disproportionately large response, causing the individual to be startled into wakefulness with a fright. This

exaggerated startle response (*hyperekplexia*) can be a common experience at the end of an overnight sleep.

Following Fulcher *et al* [7], we highlight the regions of slow dynamical evolution in the Fig. 1.13 V_m-vs-D_v graph by using a grayscale representation of $\dot{V}$, the magnitude of the velocity field in V_v–V_m space,

$$\dot{V} = \left[(dV_v/dt)^2 + (dV_m/dt)^2\right]^{1/2} \tag{1.20}$$

where dV_v/dt and dV_m/dt are defined respectively by the VLPO and MA equations of motion Eqs (1.16, 1.17). The grayscale shading shows that the regions of slow evolution form a penumbra that brackets the reverse-S locus of fixed points. The low-$\dot{V}$ penumbral region is particularly accentuated in the vicinity of the saddle–node turning points, defining saddle–node remnants or *ghosts* [26]. The wake-ghost (to the right of SN_1) and the sleep-ghost (to the left of SN_2) act as low-velocity bottlenecks, so any trajectory entering a ghostly region will tend to linger there, exhibiting low-frequency enhancement of noise-induced voltage fluctuations as it traverses the bottleneck. This suggests that the region of sleep-onset hypersensitivity to impulsive stimuli could persist beyond the immediate proximity of the wake-branch critical point to include the shadow zone defined by the wake-ghost.

1.6 Discussion

In this chapter we have examined several mathematical models for state transitions in single neurons and in neural populations. The change of state occurs when a control parameter (such as stimulus current, anesthetic concentration, neuromodulator concentration) crosses a critical threshold, causing the initial equilibrium state to lose stability, typically via a saddle–node or a Hopf bifurcation. We can detect proximity to criticality by adding a small white-noise perturbation to induce fluctuations in the observed variable, such as the membrane voltage, allowing the system to explore its nearby state-space. As the system approaches the instability point, the fluctuations grow in amplitude and in spectral coloration with a power-law divergence that depends on the nature of the instability.

For a Hopf bifurcation, the fluctuation power diverges as $1/\varepsilon$ (where ε is the displacement of the control parameter from threshold), and the spectral content becomes "critically tuned" at a nonzero resonance frequency ω_o with the power spectral density scaling as $1/(\omega - \omega_o)^2$. This is the behavior seen in the subthreshold oscillations of the H.R. Wilson type-II resonator membrane.

For a saddle–node bifurcation, the fluctuation power scales as $1/\sqrt{\varepsilon}$, and the spectral power scales as $1/\omega^2$, implying infinite power at zero frequency. The divergence at dc is the source of the critical slowing seen in the noise-induced fluctuations as a saddle–node annihilation point is approached. This behavior was demonstrated in the type-I integrator neuron, and in the mean-field models for anesthetic

induction, SWS-to-REM sleep cycling, and in the FPR model for the wake-to-sleep transition.

We argue that the presence of a neural instability provides a natural demarcation point separating two distinct states, and that a transit across this boundary can be viewed as a phase transition between states. Guedel's observation [9] of an ether-induced delirium phase—separating relaxed consciousness from anesthetic unconsciousness—provided the first historical hint that induction of anesthesia is a brain phase transition. The suppression of bacterial luminescence by volatile agents (ether, chloroform, halothane, nitrous oxide) at clinically relevant concentrations [10,28] lead to the paradoxical finding of large fluctuations in light intensity at low drug concentrations, consistent with a Guedel-like excited "delirium" phase in bacterial activity. Recent measurements of patient response to the injectable agent propofol show similar "biphasic" (surge followed by decay) brain EEG activity during induction of anesthesia [14, 15], with a second biphasic surge occurring as the patient recovers consciousness. The observation of a hysteresis separation between the induction and emergence biphasic peaks (the recovery biphasic peak occurs at a *lower* drug concentration) suggests that induction of anesthesia can be pictured as a first-order phase transition.

Examination of EEG traces for sleeping mammals (human, cat, fetal sheep) shows broad similarities in sleep patterns, with periodic alternations between a slow, large-amplitude phase (SWS), and a desynchronized lower-amplitude phase (REM sleep). The growth in low-frequency power prior to transition into REM sleep is consistent with the SWS-to-REM sleep phase transition being first-order; the absence of a correlated power surge for REM-to-SWS suggests that this transition is continuous.

The FPR phase transition model for the diurnal transition between wake and sleep is based on mutual inhibition of the VLPO and MA brainstem nuclei, resulting in hysteretic flip-flop bistability between wake and sleep states. Each state loses stability via a saddle–node annihilation, so critically-slowed voltage fluctuations, with attendant nonlinear increases in stimulus susceptibility, are predicted in the vicinity of state change. This hypersensitivity to stimulus might provide a natural explanation for the disconcerting hypnic jerk events that are commonly experienced at the moment of sleep onset.

Acknowledgements This research was supported by the Royal Society of New Zealand Marsden Fund, contract UOW-307. We are grateful for assistance from I.P. Gillies, Yanyang Xu, and J.J. Wright.

References

1. Carmichael, H.: Statistical Methods in Quantum Optics: Master Equations and Fokker–Planck Equations. Springer, Berlin New York (1999)
2. Destexhe, A., Contreras, D., Steriade, M.: Spatiotemporal analysis of local field potentials and unit discharges in cat cerebral cortex during natural wake and sleep states. J. Neurosci. **19**(11),

4595–4608 (1999)
3. Eilers, P.H.C.: Smoothing and interpolation with finite differences. In: P.S. Heckbert (ed.), Graphic Gems IV, pp. 241–250, Academic Press, San Diego, CA, USA (1994)
4. Franks, N.P., Lieb, W.R.: Anaesthetics set their sites on ion channels. Nature **389**, 334–335 (1997)
5. Freeman, W.J.: Mass Action in the Nervous System. Academic Press, New York (1975)
6. Freeman, W.J.: Neurodynamics, volume transmission, and self-organization in brain dynamics. J. Integ. Neurosci. **4**(4), 407–421 (2005)
7. Fulcher, B.D., Phillips, A.J.K., Robinson, P.A.: Modeling the impact of impulsive stimuli on sleep-wake dynamics. Phys. Rev. E **78**(5), 051920 (2008), doi:10.1103/PhysRevE.78.051920
8. Gardiner, C.W.: Handbook of Stochastic Methods for Physics, Chemistry, and the Natural Sciences, vol. 13 of Springer Series in Synergetics. Springer-Verlag, Berlin Heidelberg New York, 3 edn. (2004)
9. Guedel, A.E.: Inhalational Anesthesia: A Fundamental Guide. Macmillan, New York (1937)
10. Halsey, M.J., Smith, E.B.: Effects of anaesthetics on luminous bacteria. Nature **227**, 1363–1365 (1970)
11. Hodgkin, A.L., Huxley, A.F.: A quantitative description of membrane current and its application to conduction and excitation in nerve. J. Physiol. (Lond.) **117**, 500–544 (1952)
12. Izhikevich, E.M.: Neural excitability, spiking, and bursting. Internat. J. Bifur. Chaos **10**, 1171–1266 (2000)
13. Kitamura, A., Marszalec, W., Yeh, J.Z., Narahashi, T.: Effects of halothane and propofol on excitatory and inhibitory synaptic transmission in rat cortical neurons. J. Pharmacol. **304**(1), 162–171 (2002)
14. Kuizenga, K., Kalkman, C.J., Hennis, P.J.: Quantitative electroencephalographic analysis of the biphasic concentration–effect relationship of propofol in surgical patients during extradural analgesia. British Journal of Anaesthesia **80**, 725–732 (1998)
15. Kuizenga, K., Proost, J.H., Wierda, J.M.K.H., Kalkman, C.J.: Predictability of processed electroencephalography effects on the basis of pharmacokinetic–pharmacodynamic modeling during repeated propofol infusions in patients with extradural analgesia. Anesthesiology **95**, 607–615 (2001)
16. Liley, D.T.J., Cadusch, P.J., Wright, J.J.: A continuum theory of electro-cortical activity. Neurocomputing **26–27**, 795–800 (1999)
17. Oswald, I.: Sudden bodily jerks on falling asleep. Brain **82**, 92–103 (1959)
18. Phillips, A.J.K., Robinson, P.A.: A quantitative model of sleep-wake dynamics based on the physiology of the brainstem ascending arousal system. J. Biol. Rhythms **22**(2), 167–179 (2007), doi:10.1177/0748730406297512
19. Phillips, A.J.K., Robinson, P.A.: Sleep deprivation in a quantitative physiologically-based model of the ascending arousal system. J. Theor. Biol. **255**, 413–423 (2008), doi: 10.1016/j.jtbi.2008.08.022
20. Rechtschaffen, A., Kale, A.: A Manual of Standardized Terminology, Techniques, and Scoring System for Sleep Stages of Human Subjects. U.S. Govt Printing Office, Washington DC (1968)
21. Steyn-Ross, D.A., Steyn-Ross, M.L., Sleigh, J.W., Wilson, M.T., Gillies, I.P., Wright, J.J.: The sleep cycle modelled as a cortical phase transition. Journal of Biological Physics **31**, 547–569 (2005)
22. Steyn-Ross, D.A., Steyn-Ross, M.L., Wilson, M.T., Sleigh, J.W.: White-noise susceptibility and critical slowing in neurons near spiking threshold. Phys. Rev. E **74**, 051920 (2006)
23. Steyn-Ross, M.L., Steyn-Ross, D.A., Sleigh, J.W.: Modelling general anaesthesia as a first-order phase transition in the cortex. Progress in Biophysics and Molecular Biology **85**, 369–385 (2004)
24. Steyn-Ross, M.L., Steyn-Ross, D.A., Sleigh, J.W., Liley, D.T.J.: Theoretical electroencephalogram stationary spectrum for a white-noise-driven cortex: Evidence for a general anesthetic-induced phase transition. Phys. Rev. E **60**, 7299–7311 (1999)

25. Steyn-Ross, M.L., Steyn-Ross, D.A., Sleigh, J.W., Wilcocks, L.C.: Toward a theory of the general anesthetic-induced phase transition of the cerebral cortex: I. A statistical mechanics analogy. Phys. Rev. E **64**, 011917 (2001)
26. Strogatz, S.H.: Nonlinear Dynamics and Chaos. Westview Press, Cambridge, MA (2000)
27. Ueda, I.: Effects of diethyl ether and halothane on firefly luciferin bioluminescence. Anesthesiology **26**, 603–606 (1965)
28. White, D.C., Dundas, C.R.: The effect of anaesthetics on emission of light by luminous bacteria. Nature **226**, 456–458 (1970)
29. Wilson, H.R.: Simplified dynamics of human and mammalian neocortical neurons. J. Theor. Biol. **200**, 375–388 (1999)
30. Wilson, H.R.: Spikes, Decisions and Actions: The Dynamical Foundations of Neuroscience. Oxford University Press, New York (1999)

Index